The K-profile Parameterization augmented by Deep Neural Networks (KPP_DNN) in the General Ocean Turbulence Model (GOTM)

Jianguo Yuan[1], Jun-Hong Liang[1,2], Eric P. Chassignet[3], Olmo Zavala-Romero[3], Xiaoliang Wan[2,4] and Meghan F. Cronin[5]

[1]Department of Oceanography & Coastal Sciences, Louisiana State University, Baton Rouge, LA

[2]Center for Computation and Technology, Louisiana State University, Baton Rouge, LA

[3]Center for Ocean-Atmospheric Prediction Studies, Florida State University, Tallahassee, FL

[4]Department of Mathematics, Louisiana State University, Baton Rouge, LA

[5]NOAA Pacific Marine Environmental Laboratory (PMEL), Seattle, WA

Corresponding author: Jun-Hong Liang (jliang@lsu.edu)

Key Points:

- K-Profile Parameterization schemes, augmented by Deep Neural Networks (KPP_DNN), have been developed and trained using Large Eddy Simulations.
- The KPP_DNN schemes have been implemented in the General Ocean Turbulence Model (GOTM).
- The KPP_DNN schemes are stable for long-term integration and as efficient as the physics-based KPP schemes.

Abstract

This study utilizes Deep Neural Networks (DNN) to improve the K-Profile Parameterization (KPP) for the vertical mixing effects in the ocean's surface boundary layer turbulence. The DNNs were trained using 11-year turbulence-resolving solutions, obtained by running a large eddy simulation model for Ocean Station Papa, to predict the turbulence velocity scale coefficient and unresolved shear coefficient in the KPP. The DNN-augmented KPP schemes (KPP_DNN) have been implemented in the General Ocean Turbulence Model (GOTM). This implementation is stable for long-term integration and as efficient as existing variants of KPP schemes. Three different KPP_DNN schemes, varying in input and output variables, have been developed and trained. The performance of models using the KPP_DNN schemes is compared with that of those using popular deterministic first-order and second-moment closure turbulent mixing parameterizations. Solution comparisons show that the simulated mixed layer is cooler and deeper, aligning closely with observations when wave effects are included in parameterizations. In the KPP framework, changes to the velocity scale of unresolved shear, which is used to calculate mixed layer depth, have a larger impact on the simulated mixed layer than do changes to the magnitude of diffusivity. In the KPP_DNN, changes to unresolved shear depend on not only on wave forcing, but also on the mixed layer depth and buoyancy forcing.

Plain Language Summary

The uppermost tens of meters of the ocean, known as the ocean surface boundary layer, are rich in intricate and chaotic fine-scale (cm to 100s m) ocean currents referred to as turbulence. These currents, spanning from centimeters to hundreds of meters, play pivotal roles in shaping the oceanic environment and influencing Earth's climate dynamics. Despite their

significance, accurately simulating these fine-scale ocean currents remains beyond the capabilities of current and foreseeable supercomputing resources. Consequently, simplified formulas derived from fundamental principles are commonly employed to approximate these currents in ocean and climate models. However, these approximations still cannot cover all types of choppy currents and uncertainties in these approximations represent a substantial source of bias in contemporary ocean and climate modeling endeavors. In this study, we enhance one of the prevalent physics-based approximations of fine-scale turbulent currents using machine learning techniques. Our tests show that integrating machine learning in physics-based approximation is stable and efficient and is suitable for use in ocean and climate models.

1 Introduction

The ocean surface boundary layer (OSBL) is a thin layer below the ocean surface, typically extending tens to a hundred meters in thickness, and is strongly affected by external forcing such as wind, waves, and net heat fluxes. Ocean currents within the OSBL are highly turbulent, with the scale of these turbulent currents ranging from centimeters to several hundred meters. These turbulent currents have a profound impact on ocean dynamics, both within and beyond the OSBL, playing a significant role in sustaining marine ecosystems and shaping global climates. However, despite advances in oceanography, accurately simulating these turbulent processes remains a formidable challenge, particularly in regional and global ocean models, where directly resolving these dynamics is computationally infeasible in the foreseeable future (Fox-Kemper et al., 2019; Fox-Kemper et al., 2014).

In realistic ocean and climate models, the turbulent flux of a variable x, i.e., $\overline{w'x'}$, is calculated as:

$$\overline{w'x'} = -K_x \frac{\partial \overline{x}}{\partial z} \quad (1)$$

Here, x represents a property in ocean water such as momentum, temperature, or material concentrations; z is the vertical coordinate; and w is the vertical velocity of water. The overbar in equation 1 represents the ensemble average, while the prime denotes the turbulent fluctuation, i.e., $x' = x - \overline{x}$. K_x in equation 1 is the eddy viscosity or diffusivity, represented by simplified physics-based formulas called parameterizations. These parameterizations incorporate empirical, tunable coefficients. In early studies, the coefficients were tuned using in situ observations of temperature and salinity (e.g., Large et al., 1994) . However, in-situ observations are modulated by turbulent currents as well as submesoscale to large-scale currents. Over the past 20 years, turbulence-resolving simulations of OSBL turbulence, using Large Eddy Simulation (LES) models, have become available, with LES solutions being used to derive empirical parameters (e.g., Harcourt, 2015; van Roekel et al., 2012). LES models simulate OSBL turbulence exclusively, excluding submesoscale to large-scale processes, thus are superior to tune parameterizations of turbulent mixing.

Turbulent mixing parameterization schemes typically fall into two categories. The first category is the first-order closure scheme, in which parameters are directly related to the forcing conditions and water property profiles. A well-known example is the K-profile parametrization (KPP) scheme. The KPP scheme was initially proposed for turbulence in atmospheric boundary layers (Troen & Mahrt, 1986) and later adapted for the OSBL (Large et al., 1994). Due to its computational efficiency and stability, the KPP scheme is widely used in realistic simulations for regional and global oceans (e.g., Belcher et al., 2012; Y. Li et al., 2017; Liang et al., 2022; McWilliams & Sullivan, 2000; van Roekel et al., 2018; van Roekel et al., 2012; Vertenstein et

al., 2012; Warner et al., 2005). The second category is the second-momentum closure (SMC) scheme, where turbulent diffusivity and turbulent viscosity are derived from turbulence statistics (kinetic energy, length scale, and dissipation rate) and empirically calculated in the scheme (Kantha & Clayson, 1994; Reichl & Hallberg, 2018; Umlauf & Burchard, 2003). The SMC scheme, being computationally more expensive than the KPP scheme, is more commonly used in simulations of coastal oceans, where the current environment is more complicated (e.g., Warner et al., 2005) than in global and regional oceans. Recent studies have revised both the KPP and SMC schemes to include enhanced turbulent mixing effect due to wave-driven Langmuir turbulence, i.e., KPPLT and SMCLT. Studies have shown that the use of KPPLT and SMCLT generally improves the simulations of sea surface temperature and the mixed layer depth (MLD) for global (Q. Li et al., 2016) and regional oceans (Ali et al., 2019). However, a recent study (Q. Li et al., 2019) examining 11 mixing parameterization schemes, including KPP, SMC, KPPLT, and SMCLT, found substantial differences in the solutions provided by these methods, indicating persistent biases across all schemes.

Further refining traditional turbulent mixing parameterizations is challenging. In the upper ocean, turbulent mixing is driven by diverse combinations of wind, wave, and buoyancy conditions. However, deterministic parameterization schemes were developed based on a small subset of the realistic conditions across the global ocean (e.g., Fig.1 in Q. Li et al., 2019). Furthermore, deterministic formulas for empirical coefficients lack the flexibility to account for the vast combinations of wind, wave, and buoyancy conditions.

In light of these challenges, recent efforts have begun exploring alternative approaches to take advantage of the recent development of machine learning techniques, especially deep neural networks (DNNs), to enhance the representation of the mixing effects of OSBL turbulence.

DNNs utilize extensive data as truth to establish non-linear relationships between the inputs and predicted outcomes. Early attempts aimed to replace traditional mixing parameterization by directly predicting turbulent fluxes using DNNs (e.g., Gentine et al., 2018; Liang et al., 2022; Rasp et al., 2018). While these DNNs have shown promising results in predicting turbulent flux profiles, ensuring numerical stability when integrating them with realistic climate models for long-term use poses challenges (Rasp, 2020).

An alternative approach is to retain the physics-based framework in traditional parameterizations and use DNN to predict parameters that are uncertain in those parameterizations. Sane et al. (2023) trained DNNs to predict profiles of eddy diffusivity in the OSBL under the framework of the energetics-based planetary boundary layer (ePBL, Reichl & Hallberg, 2018) using simulations based on a SMC scheme as the truth. The authors further coupled the ePBL-DNN model into the Modular Ocean Model (MOM, e.g., Adcroft et al., 2019), and demonstrated its stability for long-term integration. Zhu et al. (2022) trained DNNs to predict mixing coefficients in the interior ocean (below the OSBL) based on in-situ microstructure observations at the equatorial Pacific Ocean. By implementing it into the MOM, they demonstrated that incorporating a DNN into the model reduces cold biases in the equatorial Pacific. The study, however, did not attempt to improve parameterizations on the effects of OSBL turbulence.

However, the DNN models in those two studies are not based on LES solutions and have not targeted the popular KPP model. In this study, we aim to bridge the gap by using high-resolution LES simulations to develop DNN models capable of predicting key turbulent mixing parameters in the widely used KPP model. The models in this study are designed to enhance the realism of OSBL simulations within the framework of the KPP scheme, without altering

fundamental equations or time-stepping mechanisms, thus facilitating straightforward integration into existing ocean models. The rest of the paper is organized as follows: Section 2 presents the framework of the DNN-augmented KPP (KPP_DNN) and outlines the data used to train the DNNs. Section 3 provides details on the implementation of the DNN-augmented KPP schemes into the General Ocean Turbulence Model (GOTM). Section 4 describes how the GOTM is configured with traditional physics-based parameterization and KPP_DNN. Section 5 evaluates the performance of KPP_DNN in comparison to traditional parameterization schemes. Section 6 summarizes the major findings of the study.

2 The K-Profile Parameterization augmented by Deep Neural Networks (KPP_DNN)

2.1 Model Description

In the KPP framework (Large et al., 1994), the expression for viscosity or diffusivity K_x is given by:

$$K_x(\sigma) = w_x(\sigma)hG_x(\sigma) \quad (2)$$

Here, w_x is a velocity scale related to the surface forcing and the Monin-Obukhov similarity theory, h is the surface boundary layer depth, and $G_x(\sigma)$ is a dimensionless shape function, with $\sigma = z/h$ the depth normalized by h. The OSBL depth h is the depth to which OSBL turbulence reaches. In low and mid-latitudes, where mixed layers are relatively shallow, the OSBL depth equals the MLD. In high-latitude oceans where the mixed layer is deep, the OSBL is limited by the earth's rotation and is thinner than the mixed layer.

In mixing parameterizations, the OSBL depth h is typically diagnosed by identifying the depth at which the Richardson number (*Ri*), a measure of the relative importance between shear and stable stratification, exceeds a critical value Ri_c. This criterion is based on linear stability

analysis, which shows that stably stratified shear flow is unstable and turbulent mixing quenches when the gradient *Ri* exceeds a critical value of 0.3, i.e., $Ri > Ri_c = 0.3$. Below the OSBL depth, *Ri* is larger than Ri_c and the flow is stable. Above the depth, *Ri* is smaller than Ri_c and the flow is turbulent. In the KPP scheme, the bulk Richardson number $Ri_b(z)$ is used and the critical bulk Richardson number is set to be 0.3 (Large et al., 1994). $Ri_b(z)$ is related to ocean current and stratification as,

$$Ri_b(z) = \frac{z\left(b_r - \overline{b(z)}\right)}{\left(\boldsymbol{u}_r - \overline{\boldsymbol{u}(z)}\right)^2 + U_t^2(z)} \tag{3}$$

Here, b is the buoyancy, defined as $b = g[\alpha_\theta(\theta - \theta_r) - \beta_s(s - s_r)]$, with θ the potential temperature, s the salinity, α_θ and β_s the corresponding thermal and saline expansion coefficients, respectively; $\boldsymbol{u}$ is the water current vector. The subscript r denotes the vertically averaged value over the surface layer. The effect of turbulence is represented using the velocity scale of the unresolved shear $U_t^2(z)$:

$$U_t^2(z) = \frac{C_v N(z) w_x(z)|z|}{Ri_c} \tag{4}$$

where C_v is a dimensionless coefficient and N is the Brunt-Väsälä frequency.

Recent studies have shown that the effects of non-breaking waves greatly modulate turbulent fluxes in the OSBL, either enhancing or suppressing turbulent fluxes depending on the alignment between wind and waves (McWilliams et al., 2014; van Roekel et al., 2012). When wind and waves are largely aligned, as is common across the global ocean, turbulence is enhanced by wave-driven Langmuir turbulence. When waves are significantly misaligned with the wind, as occurs when the swell is strong, turbulence is suppressed. Several recent studies (e.g., Q. Li & Fox-Kemper, 2017; Q. Li et al., 2019; McWilliams & Sullivan, 2000; van Roekel et al., 2012) have been devoted to including wave effects into the KPP framework. In those

parameterizations, referred to as KPPLT hereafter, the turbulent velocity scale (w_x), and the unresolved shear velocity scale, $U_t^2(z)$, are modified as,

$$K_x(\sigma) = \epsilon w_x(\sigma)|h|G_x(\sigma) \tag{5}$$

$$U_t^2(z) = \eta U_t^2(z)|_{LMD} \tag{6}$$

where $U_t^2(z)|_{LMD}$ is the term calculated using a formula in Large et al. (1994), the velocity scale coefficient ϵ and the unresolved shear coefficient η are deterministic functions of wind and wave forcing (e.g., Q. Li & Fox-Kemper, 2017; Reichl et al., 2016)

In this study, these two coefficients will be determined by Deep feedforward Neural Networks (DNNs), as opposed to deterministic functions in deterministic formulas in existing studies. The DNN augmented parameterization will be called KPP_DNN hereafter.

A DNN is made up of multiple densely connected layers, including one input layer, one output layer, and multiple hidden layers (Figure 1). Each layer includes multiple neurons. Neurons between layers are connected by the following relationship:

$$X_{i,j} = f\left(\sum_{k=1}^{N_{j-1}} w_{k,i,j-1} X_{k,j-1} + b_{k,i,j-1}\right) \tag{7}$$

where $X_{i,j}$ means the ith neuron in the jth layer, N_j is the number of neurons in the jth layer. $w_{k,i,j-1}$ and $b_{k,i,j-1}$ are the weight and bias that link neuron $X_{k,j-1}$ to neuron $X_{i,j}$, respectively. In this study, the Leaky Rectified Linear Unit function (Leaky ReLU, $\alpha(x) = \max(0.1x, x)$) is used as the activation function.

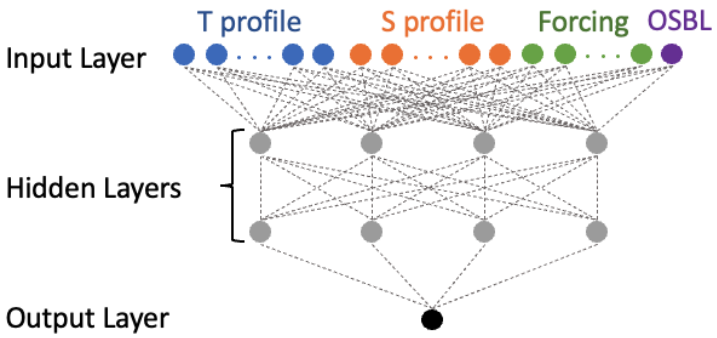

Figure 1. The architect of a Deep Neural Network (DNN) model

The DNN's input layer consists of water-column variables, including potential temperature profiles (θ), salinity profiles (s), ocean currents, and key OSBL turbulence drivers, including wind stress (τ_x, τ_y), shortwave radiation at the ocean surface (S_w), net heat flux excluding short wave radiation (Q_f), the rate of evaporation minus precipitation (Q_s), vertical profiles of Stokes drift associated with ocean surface waves and the OSBL depth from the previous time step. The output layer consists of a single neuron in each DNN model, predicting a specific parameter. Specifically, we have two different DNN models based on the output: model D_ϵ to predict the turbulent velocity scale coefficient (ϵ), and model D_η to predict the unresolved shear coefficient (η).

The DNN model utilizes a vast array of computations characterized by nonlinear activation functions with distinct weights and biases. Integrating a well-tuned DNN model into a traditional physics-based parameterization scheme not only preserves the computational stability and efficiency of a traditional physics-based model but also enables a more flexible and effective non-linear mapping from input variables to output parameters than what deterministic formulas could achieve.

211 ### 2.2 Data Generation and Curation

212 The data used to develop and test the KPP_DNN schemes are turbulence-resolving
213 simulations for Ocean Station Papa (OSP) using the NCAR-LES model for the OSBL (e.g.,
214 Sullivan & McWilliams, 2010). OSP ($50°N, 145°W$, see Figure 2a) is located within the
215 Northern Pacific subpolar gyre. With a long history of continuous atmospheric and
216 oceanographic in-situ observations (Cronin et al., 2023; Whitney & Tortell, 2006), OSP has been
217 served as a pivotal site for monitoring ocean climate (e.g., Bond et al., 2015; R. E. Thomson &
218 Tabata, 1987), understanding ocean physical and biogeochemical processes, and developing
219 parameterization schemes extensively employed in diverse ocean models (e.g., Chalikov, 2005;
220 Craig & Banner, 1994; Gaspar et al., 1990; Kantha & Clayson, 1994; Large et al., 1994). Figures
221 2b and 2c present the probability of OSBL turbulence regime at OSP based on the observed
222 forcing conditions. The most common turbulence regime at OSP is a mix of the three types of
223 turbulence. There are periods when Langmuir turbulence dominates, while convection or shear-
224 driven turbulence seldom dominates. Different from the global ocean (compare the blue and
225 black contours), the OSBL at OSP is seldom strongly convective or strongly stabilizing. LES
226 models are currently the state-of-the-art tool to study OSBL and submsoscale turbulence (e.g.,
227 Bodner et al., 2020; Fan et al., 2018; Kukulka et al., 2009; Skyllingstad & Denbo, 1995; Yuan &
228 Liang, 2021), and to develop parameterizations for those processes (e.g., Bodner et al., 2023;
229 Liang et al., 2013; Liu et al., 2022; Sinha et al., 2015).

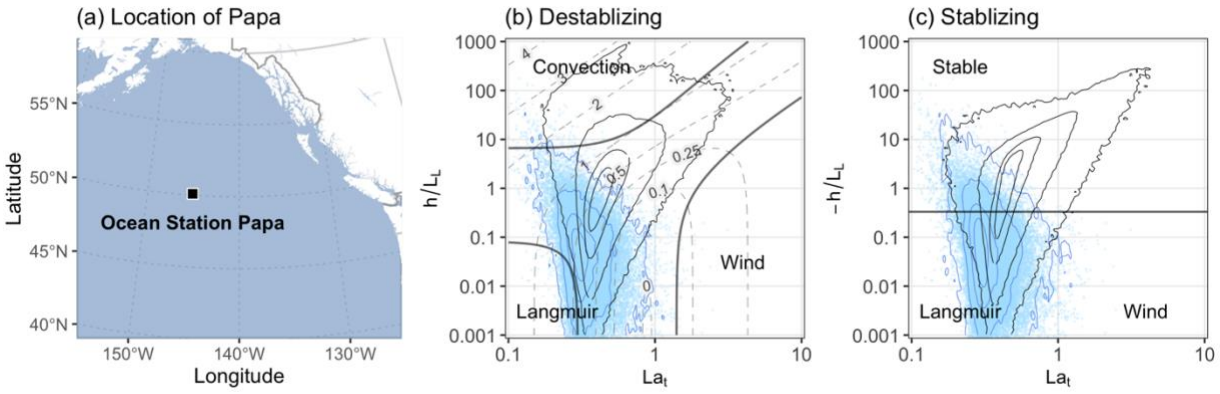

Figure 2. Panel (a) shows the location of Ocean Station Papa in the north Pacific Ocean. Panels (b) and (c) are regime diagrams showing the forcing conditions at OSP between 2010 and 2022. Panel (b) corresponds to conditions of destabilizing net surface buoyancy forces, whereas panel (c) is for conditions under stabilizing buoyancy forces. The thin solid contours are the probability (30%, 60%, 90% and 99%) of a certain parameter combination in the global ocean. The light black dots are the conditions in OSP, while the dark blue contours are the probability (30%, 60%, 90% and 99%) in OSP. In panel (b), the thin dashed contours show turbulent dissipation rate, and the thick solid grey lines encompass regimes where one of the three types of turbulence contributes over 90% to total dissipation. In panel (c), the thick grey line is the maximum equilibrium $-h/L_L$ value according to Pearson et al. (2015).

The use of the NCAR-LES model to generate data is similar to that reported in Liang et al. (2017) and Liang et al. (2022): The domain of the LES model is configured with 160 uniformly distributed grids, spanning 300m in each horizontal direction, Vertically, the LES model features 128 stretched grids across a 200m depth, with the finest grid equal 0.2m at the ocean surface. The LES model was driven by a combination of observed hourly meteorological (Cronin et al., 2015), wave conditions (J. Thomson et al., 2013) and the derived surface flux products at OSP from September 2010 to December 2022. These inputs include wind stresses,

wave conditions, shortwave radiation, net surface heat flux (excluding shortwave radiation), and the rate of evaporation minus precipitation, at OSP from September 2010 to December 2022. Periods when the observational wave data were not available were excluded from LES simulations. The LES simulations were restarted every 10 days, and initial conditions of each restart were derived from observed water column temperature and salinity profiles linearly interpolated to LES vertical grids. The restart procedure is to ensure that the LES solutions do not deviate from the true state of the ocean, as large- and mesoscale processes that also modulate the physical states of the upper ocean at the station (Cronin et al., 2015) are not resolved by the LES model. Comparisons with observation show that the LES simulations closely align with reproduces observed upper-ocean states with this approach (see Figure 3). In total, 367 LES simulations were conducted.

The turbulence-resolving LES solution dataset differs from that used by Liang et al. (2022) in two ways: Firstly, the simulation period is longer, spanning from 2010 to 2022 in the current study, as opposed to 2010 to 2019 in Liang et al. (2022), thereby offering more data for model training and testing. Secondly, shortwave radiation penetrates the OSBL in the current study while shortwave radiation was applied only at the ocean surface in Liang et al. (2022). The shortwave radiation at depth z, $Q_{sw}(z)$, is calculated as

$$Q_{sw}(z) = Q_{sw,0}\left(r\, e^{z/\mu_1} + (1-r)\, e^{z/\mu_2}\right) \quad (8)$$

where $Q_{sw,0}$ is the net shortwave radiation at the ocean surface. $r = 0.58, \mu_1 = 0.35$ and $\mu_2 = 23$ are three empirically determined constants (Paulson & Simpson, 1977) to fit the data in Jerlov (1976). The penetrative shortwave radiation is more realistic than a surface shortwave flux. In LES simulations, the penetrating shortwave radiation led to thicker OSBLs and more modest increases in sea surface temperature when compared to simulations driven by shortwave

radiation only at the ocean surface. The use of penetrative shortwave radiation is also consistent with realistic ocean models. Therefore, the KPP_DNN trained using the set of LES solutions could be implemented into realistic ocean models.

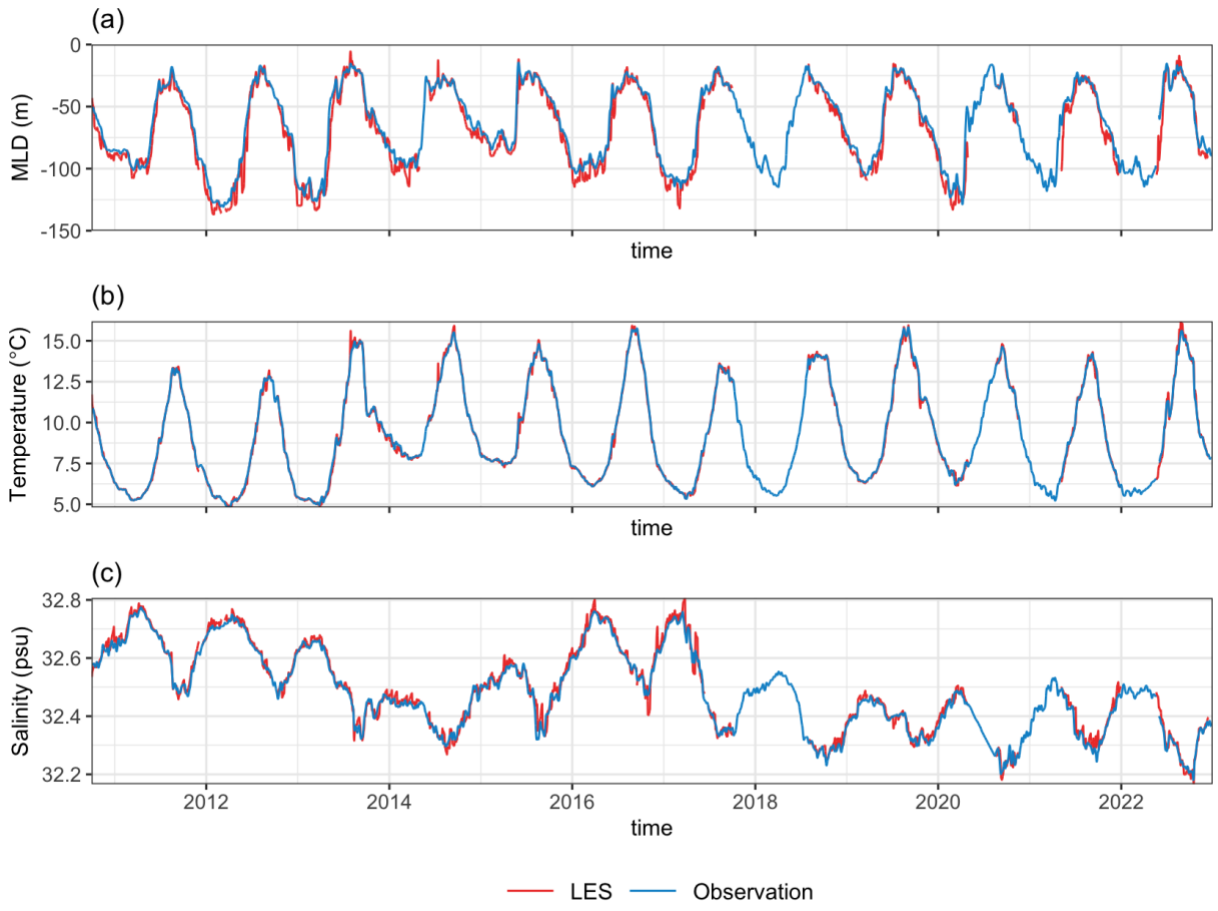

Figure 3. Comparison between the LES solutions and in situ observations in Ocean Station Papa (OSP). (a) mixed layer depth (MLD); (b) mean temperature in the mixed layer; (c) mean salinity in the mixed layer.

Ensemble-averaged profiles of temperature, salinity, velocities, turbulent kinetic energy (TKE), and their turbulent fluxes were calculated online and output every 30 minutes. The depth of the OSBL h was diagnosed as the depth at which the vertical gradient of momentum flux decreases to $2 \times 10^{-7}\ m/s^2$. η was then diagnosed using Equations 4 and 6 with a $Ri_c = 0.3$.

w_x and $G(\sigma)$ in Equation 5 were first calculated using the LES solutions and formulas detailed in Large et al. (1994). ϵ was then obtained by minimizing the difference between the momentum fluxes using equation 1 and the output momentum flux from LES solutions.

2.3 Model Training

The predicted coefficients ϵ in model D_ϵ and η in model D_η were compared with ϵ and η diagnosed from LES solutions as detailed in section 2.2. Mean square errors served as the loss to update trainable parameters in the DNNs. The DNNs were trained using TensorFlow and Keras within the R programming environment. The architecture of these DNNs varied significantly, encompassing a range of different layers (1, 2, 4, 6, 8, 12) and neurons per layer (2, 4, 8, 16, 32), to explore the optimal structure for our specific application. The Adam optimizer was employed across all models. Each model was trained for 1000 epochs. To avoid overfitting, the learning rate was reduced by a factor of 0.1 whenever a plateau in validation loss was detected during the training process. The criterion for selecting the best model was based on the smallest validation loss, a standard measure of model accuracy on unseen data, ensuring that the chosen model has the highest generalization capability.

3 Implementation of KPP_DNN in the General Ocean Turbulence Model (GOTM)

The General Ocean Turbulence Model (GOTM, Burchard et al., 1999) is a single-column model designed to examine the behavior of various turbulent mixing parameterization schemes in the OSBL. It provides a versatile framework, allowing for the straightforward compilation and execution of different OSBL turbulent mixing parameterization schemes, making it the ideal testbed for developing and testing mixing parameterizations. The current GOTM model includes

303 a variety of first-order and second-moment closure schemes, allowing for the comparison of
304 different schemes within the same framework.

305 Adding to the capability of the GOTM, this study implements the trained DNNs, their
306 structure and trainable parameters, into the model. The GOTM, like most earth system models, is
307 coded exclusively in Fortran, while DNN models are typically written in high-level
308 programming languages like Python and R, utilizing deep learning libraries such as Keras (Gulli
309 & Pal, 2017; Ketkar & Ketkar, 2017). There are two approaches that a DNN model could be
310 implemented in a Fortran code: The first is to hard-code the entire DNN structure and trainable
311 parameters directly into Fortran (e.g., Brenowitz & Bretherton, 2018; Gagne et al., 2020). The
312 other approach, adopted in this study, is to overcome the computer language interoperability by
313 incorporating a software library that connects Fortran and Python environments, such as the
314 Fortran-Keras Bridge (FKB, Ott et al., 2020) used in this study.

315 The process involves converting a trained DNN using Keras, saved in HDF format, into
316 an ASCII file offline. This ASCII file is specifically structured for easy interpretation by the
317 FKB. In a FKB informed Fortran program, the DNN model, including its structure and weights,
318 is reconstructed by loading this ASCII file. During each timestep of integration in the GOTM,
319 the necessary input array, composed of outputs from the GOTM model and forcing conditions, as
320 detailed in section 2.3, was normalized and fed into the loaded DNN model. Subsequently, the
321 DNN's predictions were then denormalized and integrated back into GOTM to compute the
322 enhancement factors in equations 6.

323 **4 Model Configurations**

324 Three different KPP_DNNs were compared against seven existing physics-based
325 parameterizations (Table 1) using the GOTM. The three KPP_DNNs vary in complexity. In

KPP_DNN1, only the coefficients for the velocity scale coefficient ϵ predicted by D_ϵ were utilized. In KPP_DNN2a, both the velocity scale coefficient ϵ predicted by D_ϵ and the unresolved shear coefficient η predicted by D_η were used. Wave-induced stokes profiles were not included as inputs of the KPP_DNN2a. KPP_DNN2b was the same as KPP_DNN2a but additionally incorporated Stokes profiles as inputs. Since most ocean models are not yet coupled with wave models, it is expected that KPP_DNN2a will be more extensively utilized in existing ocean models.

Seven well-known traditional deterministic parameterizations were also selected for comparison (Table 1). The KPP_LMD is the basis of KPP schemes and does not incorporate the enhancement of non-breaking waves. KPPLT_VR12 adds the enhancement of non-breaking wave effects only to the turbulent velocity scale but leaves the unresolved shear component unchanged. KPPLT_LF17 builds on KPPLT_VR12 and includes modification on both the velocity scale and the unresolved shear components. KPPLT_RW16 is similar to KPPLT_LF17, but formulas and coefficients that modify velocity scale and the unresolved shear were tuned using LES solutions under hurricane conditions, thus has a stronger enhancement than KPPLT_LF17. It should be noted that all three KPPLT schemes have considered the effects of wind-wave misalignment. Across the global oceans, wind and waves are often misaligned (e.g., Abolfazli et al., 2020; Hanley et al., 2010). When waves align with the wind, Langmuir turbulence enhances OSBL turbulence. When waves oppose the wind, OSBL turbulence is suppressed (e.g., McWilliams et al., 2014). All KPPLT schemes were tuned using LES solutions.

SMC_KC94 is the second closure model tuned using data over at a few different locations across the global oceans. This scheme does not include the non-breaking wave effects. SMCLT_H15 generalizes SMC_KC94 to incorporate the impact of non-breaking waves by

including the Stokes profiles in the governing equations. Coefficients in the SMCLT_H15 scheme were tuned using LES solutions.

The performance of the seven traditional parameterizations and the three variants of KPP_DNN schemes is compared using the GOTM for the year 2011 to 2016. The GOTM simulations are divided into two sets. Both sets of simulations are driven by observed meteorological and wave conditions. They differ by the surface buoyancy fluxes used to drive the model. In the first set of simulation (set 1), surface buoyancy flux products at OSP provided by Pacific Marine Environmental Laboratory (PMEL), are used as input. Those fluxes were calculated using the Coupled Ocean-Atmosphere Response Experiment (COARE) algorithm with the observed ocean and atmosphere conditions. In the second set of simulations (set 2), surface buoyancy fluxes are calculated using the same COARE algorithms online during the GOTM simulations. The online flux calculation is based on observed meteorological condition and the simulated sea surface temperature (SST) and sea surface salinity (SSS). The approach in the pre-calculated surface buoyancy flux has been commonly used in studies aiming at improving or comparing mixing parameterization schemes (e.g., Q. Li et al., 2019). In this model configuration, forcing conditions are identical among different simulations and the difference in solutions are purely due to mixing parameterizations. The online calculation of surface buoyancy flux in the second set of simulation is consistent with that in most realistic ocean simulations using regional and global models (e.g., Chassignet et al., 2020). In simulations driven by pre-calculated buoyancy fluxes, corrected fluxes to nudge the simulated SST and SSS to their climatological states are usually imposed to prevent the long-term drift in the solutions (e.g., Barnier et al., 1995). With this approach, however, the surface buoyancy flux is different among simulations using different mixing parameterizations. The GOTM simulations are restarted at the

beginning of each year using observed temperature and salinity profiles as initial conditions. In each simulation, outputs recorded at every 30 minutes. It should be noted that the GOTM with all parameterizations could be integrated for a full 6-year period without any stability issue. However, restarting at the beginning of each year mitigates the long-term drift in the solution due to the exclusion of larger-scale processes in the 1-D vertical column model (see Figure S1 in supporting information).

Table 1. List of parameterization names and the references for the deterministic parameterization schemes compared in this study.

Parameterization Name	References
KPP_LMD	Large et al. (1994)
KPPLT_VR12	van Roekel et al. (2012)
KPPLT_RW16	Reichl et al. (2016)
KPPLT_LF17	Q. Li and Fox-Kemper (2017)
SMC_KC94	Kantha and Clayson (1994)
SMCLT_H15	Harcourt (2015)

5 Results

5.1 Solution Comparisons

Figure 4 shows the evolution of surface forcing and ocean temperature profiles calculated using various mixing parameterizations for the year 2013 using pre-calculated surface buoyancy flux. Forcing conditions are identical for these solutions. Both wind and buoyancy flux exhibit distinct seasonal variability. Winds are weaker and stabilizing surface buoyancy flux prevails from March to early September than the rest of the year. During winter, there were multiple

storms characterized by short-term and significant strengthening in both wind and destabilizing surface buoyancy flux. For example, during the cold front in late September, the daily average wind speed doubled within a single day and remained above 12 m/s for approximately one week.

Figure 4b displays the temperature profiles calculated using KPP_LMD. From January to March, there is minimal variability in the simulated MLD and temperature. The simulated mixed layer was relatively deep, close to 100 m, and the mixed layer temperature was around 5°C. The upper ocean re-stratified quickly in April. The MLD shallowed from -100 m to -20 m during April. However, the warming of the mixed layer during the month is relatively modest, about 2°C. The mixed layer continued to warm, reaching a maximum temperature of 17.6°C in early September. Since then, the mixed layer cooled and deepened. It should be noted that a marine heatwave, famously known as “the Blob”, started in the winter of 2013/2014 (Bond et al., 2015; Di Lorenzo & Mantua, 2016) resulting in a shallower and warmer mixed layer at the end of 2013 than the beginning of the year. In addition to the seasonal cycle, rapid mixed layer cooling and deepening associated with storms are also evident, leading to short-term variability in both mixed layer temperature and depth. For example, storms in early June led to notable mixed layer cooling and deepening during the longer-term seasonal warming of the mixed layer during summer, while a storm in late September accelerated mixed deepening and cooling during fall.

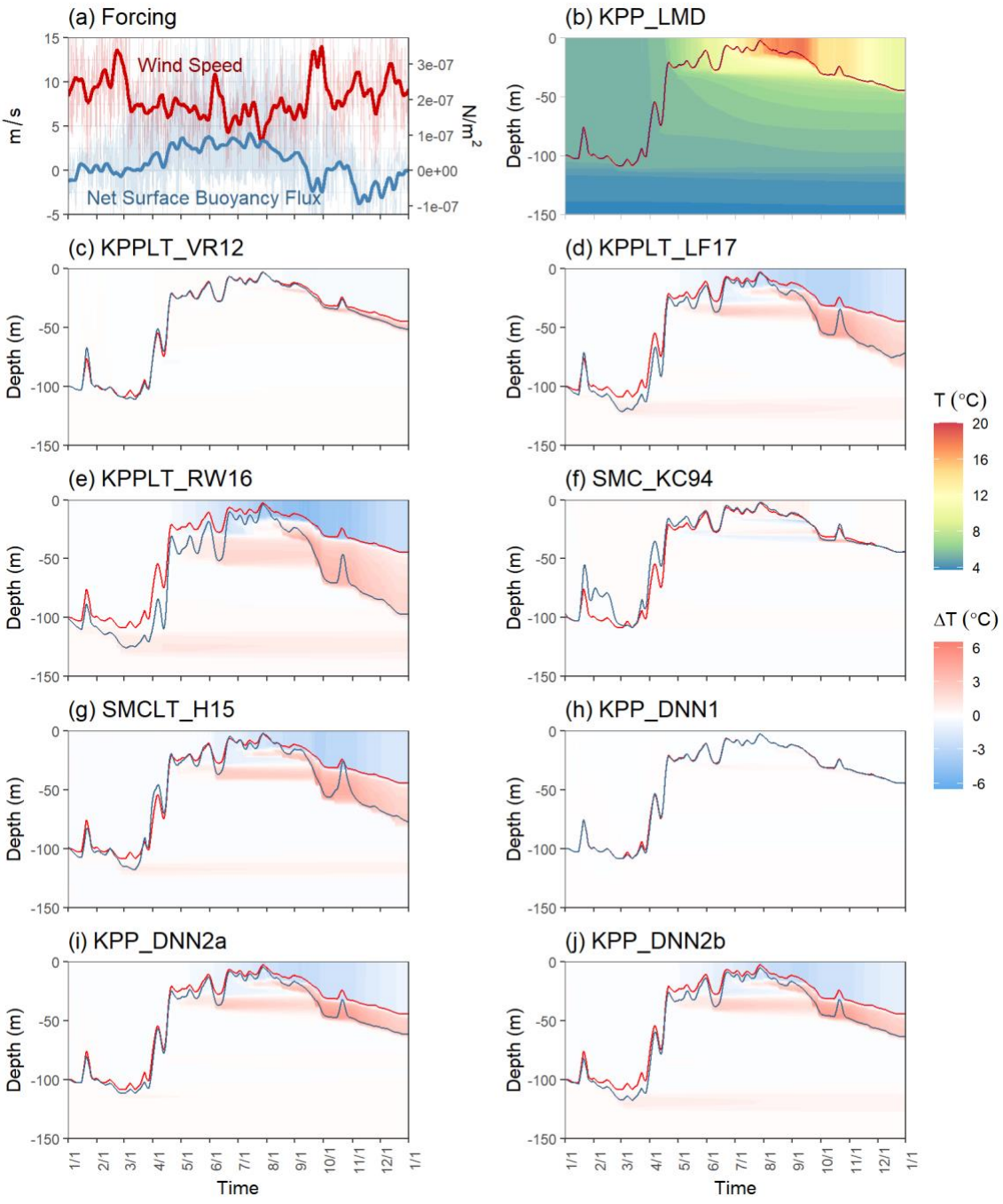

406

407 **Figure 4.** Comparison of the potential temperature profile evolutions at Ocean Station Papa in
408 the year 2013 using various simulation schemes. Forcing conditions are identical in these
409 simulations (set 1). (a) Time series for observed 10-meter wind speeds (thin red line) and net
410 surface buoyancy fluxes (thin blue line). The smoothed thick lines show the daily averaged

values. (b) potential temperature evolution calculated using KPP_LMD. Panels (c) to (j) show the difference in simulated temperature from KPP_LMD for all other parameterizations. The mixed layer depth (MLD), defined by the depth at which the density exceeds the surface value by 0.03 kg/m³, from KPP_LMD is indicated by thin red lines in panels (b) to (j), whereas the mixed layer depths from other schemes are delineated by blue lines in panels (c) to (j).

Figures 4c to 4j show the differences between different parameterizations and KPP_LMD. In KPPLT_VR12 and KPP_DNN1, wave effects are incorporated only into the velocity scale coefficient ϵ, but not in unresolved shear coefficient η. The results (Figures 4c and 4h) demonstrate only a slight impact on the simulated temperature profiles. The deviation in temperature from the baseline KPP_LMD remained relatively minor, less than 1°C throughout the year. The mixed layer was only slightly deeper after September.

In the KPP schemes that include wave effects in both velocity scale coefficient ϵ and unresolved shear coefficient η, i.e., KPPLT_LF17, KPPLT_RW16, KPP_DNN2a and KPP_DNN2b, as shown in Figures 4d, 4e, 4i and 4j, the simulated mixed layer using those schemes was evidently cooler and deeper throughout the year than that using KPP_LMD. A warm anomaly was observed at a depth of approximately 120 m throughout the year. That is the greatest depth that the mixed layer reached in March and well below the mixed layer after April when the water column re-stratified, thus highlighting the significance of OSBL mixing in shaping upper-ocean thermal profiles and heat transfer between the surface and the interior ocean. Among these solutions, the one using KPPLT_RW16 displays the most rapid mixed layer cooling and deepening in Fall, implying the strongest mixing during that period, consistent with the finding by Q. Li et al. (2019). The stronger mixing by KPPLT_RW16 is attributed to the use of hurricane conditions to tune the coefficients. The simulated short-term mixed layer cooling

and deepening due to storms, and the subsequent short-term warming and restratification by these four parameterizations were also more dramatic than those by KPP_LMD, KPPLT_VR12 and KPP_DNN1. These results highlight the importance of accounting for the unresolved shear coefficient η in modeling wave effects in parameterizations under the KPP framework.

For SMC_KC94 (Figure 4f), which did not incorporate wave effects, the simulated mixed layer tends to be shallower and warmer throughout the year compared to that in KPP_LMD, indicating that the parameterized mixing in SMC_KC94 is weaker than that in KPP_LMD. This is particularly evident during the first half of the year when the mixed layer warms and re-stratifies. With the inclusion of wave effects, the simulation using SMC_H15 yields a mixed layer that is cooler and deeper compared to the one using SMC_KC94. Between January and March, the simulated mixed layer using SMC_H15 exhibits higher temperatures than those generated by the KPPLT and KPP_DNN2 schemes. The re-stratification predicted by SMC_H15 occurs more rapidly than that by KPP_LMD, evidenced by a sharper increase in mixed layer temperature during April. The simulated mixed layer cooling and deepening rates by SMC_H15 in fall is close to those using KPPLT_LF17, KPP_DNN2a and KPP_DNN2b.

The time series of sea surface temperature (SST) for the years 2011 to 2016 are presented in Figure 5. The simulated SST is mostly warmer than observation at the end of the year for all years. At the OSP, large- and meso- scale processes also contribute to the annual cycle of SST (Cronin et al., 2015). Across the six years simulated, SST was the highest using the SMC_KC94 and the lowest using KPPLT_RW16, respectively, implying that mixing is the weakest in SMC_KC94 and is the strongest in KPPLT_RW16. When using KPPLT_VR12 and KPP_DNN1, the simulated SST is close to that in KPP_LMD throughout the 6 years, reaffirming

that KPP parameterizations without counting on wave effects on unresolved shear coefficient η has only limited impact on the evolution of MLD and temperature within the mixed layer.

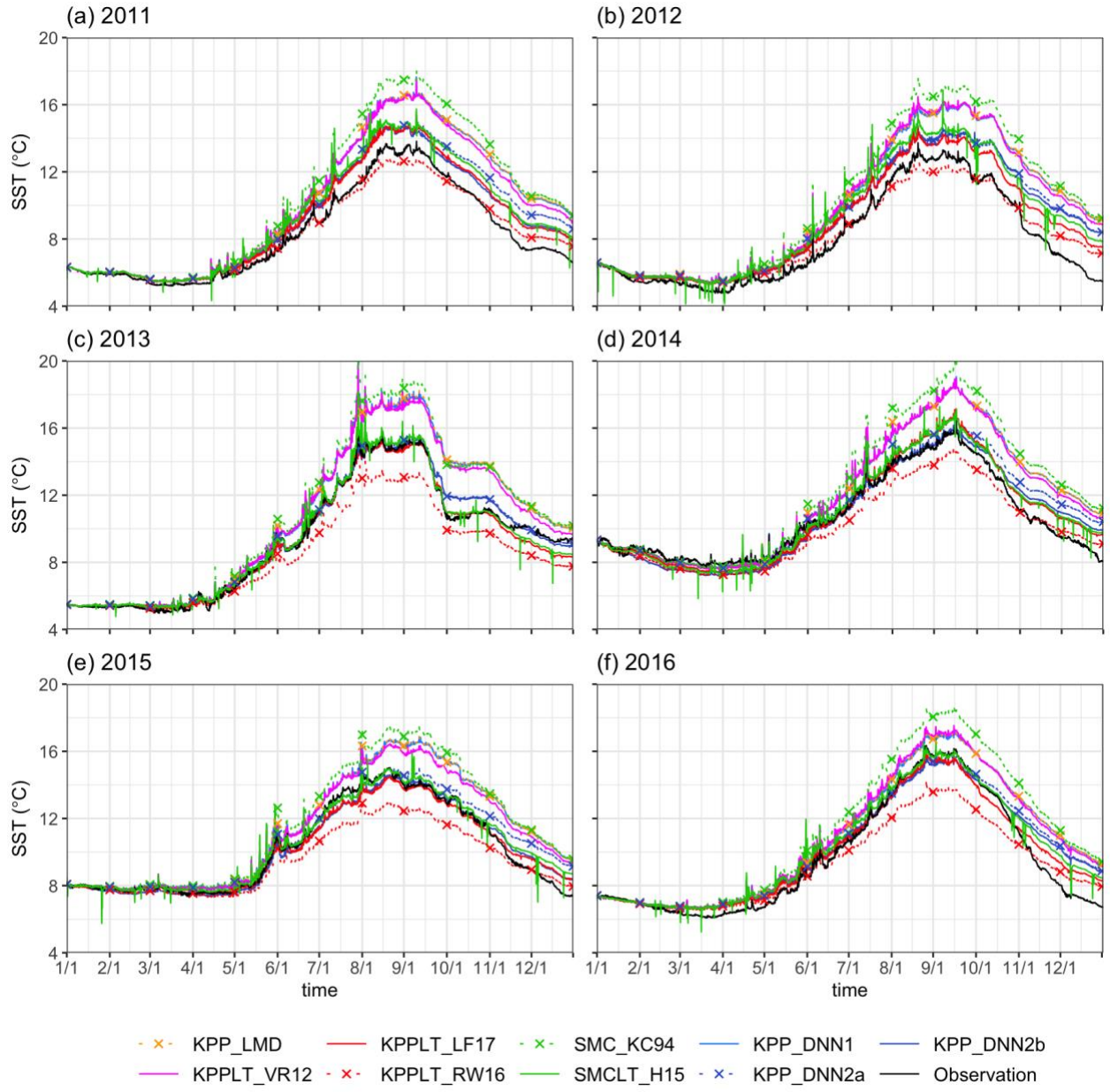

Figure 5. Comparison of observed SST time series at OSP and simulated SST time series using different schemes from 2011 to 2016 (panels (a) to (f)) in simulation Set 1. All simulations were driven by identical surface forcing conditions, i.e., using pre-calculated surface buoyancy fluxes.

462 The simulated SSTs using KPPLT_LF17, SMCLT_H15, KPP_DNN2a, and
463 KPP_DNN2b were lower than that using KPP_LMD, KPPLT_VR12, KPP_DNN1, and
464 SMC_KC94, but higher than that using KPPLT_RW16. There is a considerable difference
465 between the solutions of the two KPP_DNN2 schemes: KPP_DNN2a and KPP_DNN2b. The
466 simulated SSTs by the two schemes were close to each other for the year 2013. In other
467 simulated years, the simulated SSTs when using KPP_DNN2b were noticeably cooler than that
468 using KPP_DNN2a. The difference between KPP_DNN2a and KPP_DNN2b highlights the
469 different roles that waves played in different years.

470 The simulated SSTs using KPPLT_LF17, SMCLT_H15, KPP_DNN2a, and
471 KPP_DNN2b were more closely aligned with both the magnitude and the tendency of the
472 observed SSTs in OSP than using KPP_LMD, KPPLT_VR12, KPPLT_RW16 and SMC_KC94.
473 However, it is important to note that the one-dimensional column models like the GOTM do not
474 account for processes at a scale larger than boundary layer turbulence, such as submesoscale,
475 mesoscale, and large-scale circulations. Therefore, differences between GOTM solutions and
476 observations should be interpreted with caution as they could be due to contributions by those
477 larger-scale processes. As pointed out by Large et al. (1994), OSP is often impacted by heat
478 advection between September and February, a factor that can significantly modulate SSTs but is
479 not included in the 1D GOTM simulation, thus often causing larger discrepancies between
480 simulated and observed SSTs during these months. For example, observed cooling is stronger
481 than the simulated cooling by all schemes during November 2016 and warmer than the simulated
482 cooling by all schemes with wave effects during December 2013.

483 The simulated SSTs, derived using online flux calculation (set 2), are presented in Figure
484 6. With online flux calculation, the buoyancy fluxes vary across different simulations. A lower

simulated SST results in smaller surface heat loss, as both the outgoing long wave and the sensible heat loss calculated from the COARE algorithm are both smaller. Different from the solutions using pre-calculated fluxes (set 1) shown in Figure 5, the differences in SST among simulations employing different turbulent mixing schemes in Figure 6 were much smaller, mostly less than 0.5°C. The simulated SSTs using different parameterization schemes were also more closely aligned with observations. However, starting from November, consistent biases from the observed SSTs were found in each simulated year, with SSTs generally being higher except for the year 2013. The deviated SSTs in winter are due to the advection effects which are not considered in the 1D GOTM model, while the unique SST biases in winter 2013, is likely due to the heatwave “Blob”. These biases underscore the influence of advection on SSTs, an impact that could not be completely mitigated by online flux calculation using bulk formulas.

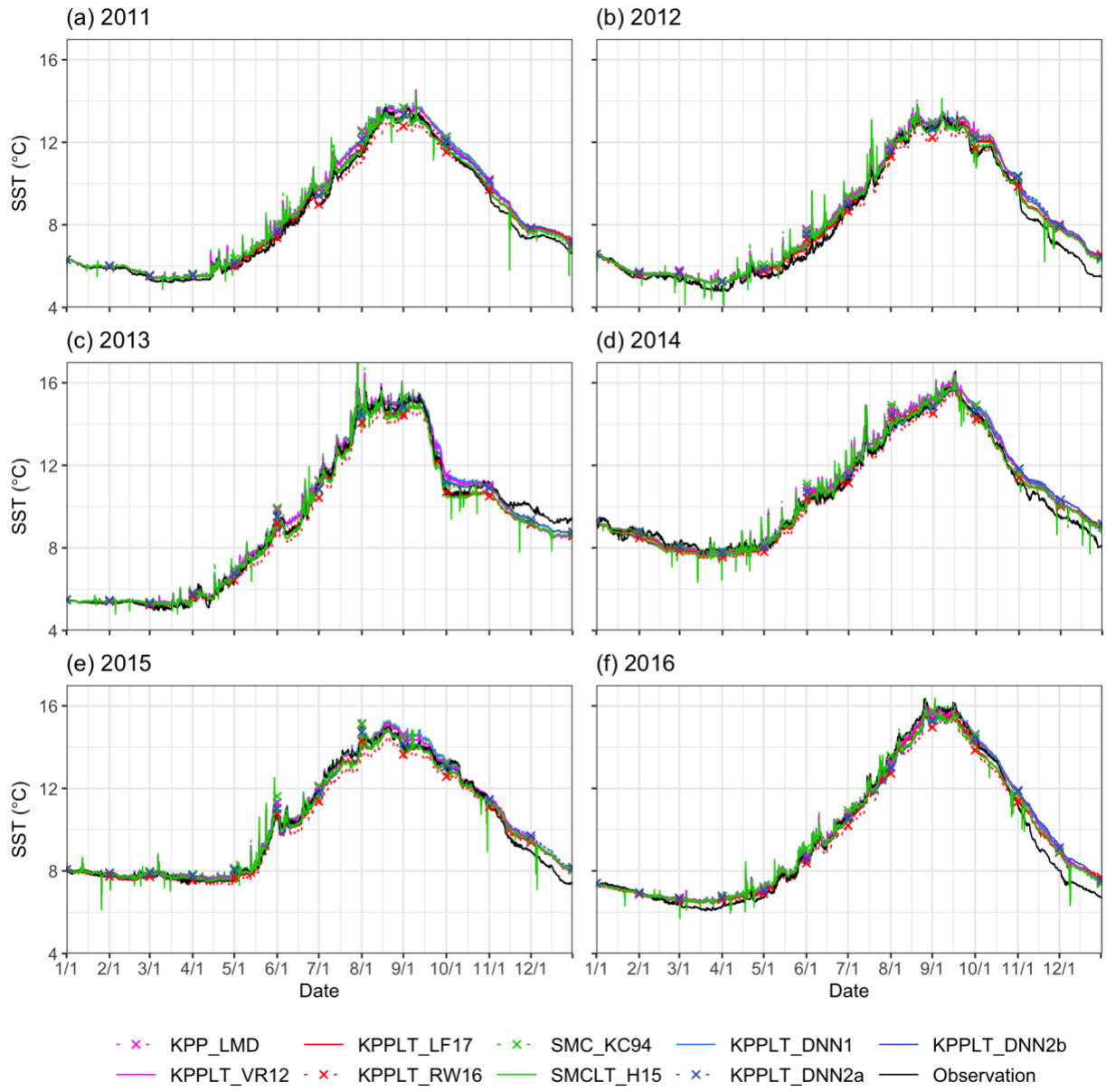

Figure. 6. Same as Figure 5, but for Simulation Set 2 using buoyancy flux calculated online.

Figure 7 shows the differences in the simulated MLDs between simulations driven by pre-calculated buoyancy fluxes (set 1) and those driven by fluxes calculated online using bulk formulas (set 2). During the summer months, , the simulated MLDs in set 1, using pre-calculated flux, were mostly slightly shallower with KPP_LMD, and slightly thicker with KPPLT_RW16 in

503 comparison with the observed MLDs. Simulated MLDs in set 2, which used online flux
504 calculation, were shallower and better aligned to observations. During this period, online flux
505 calculation reduces biases in both simulated SSTs and MLDs. However, during the colder
506 months from January to April and after November, when the simulated SST is higher than the
507 observed SST (Fig. 6), the simulated MLDs were deeper when driven by fluxes calculated online
508 using bulk formula. Note that during these periods, the MLDs in simulations using
509 parameterization schemes with wave enhancements (KPPLT_LF17, KPPLT_RW16 and
510 KPP_DNN2b) were deeper than the observed mixed layer. Results of simulations over a 6-year
511 period from 2011 to 2016 (see Figure S1 in supporting information) confirms that all the
512 simulations using online flux calculation efficiently eliminates the warming drift of SSTs, but the
513 deviations of MLDs in colder months amplified over years, even for KPP_LMD. While the
514 online flux calculation has the potential to reduce biases in the simulated SST, it could
515 conversely increase biases in the simulated MLDs.

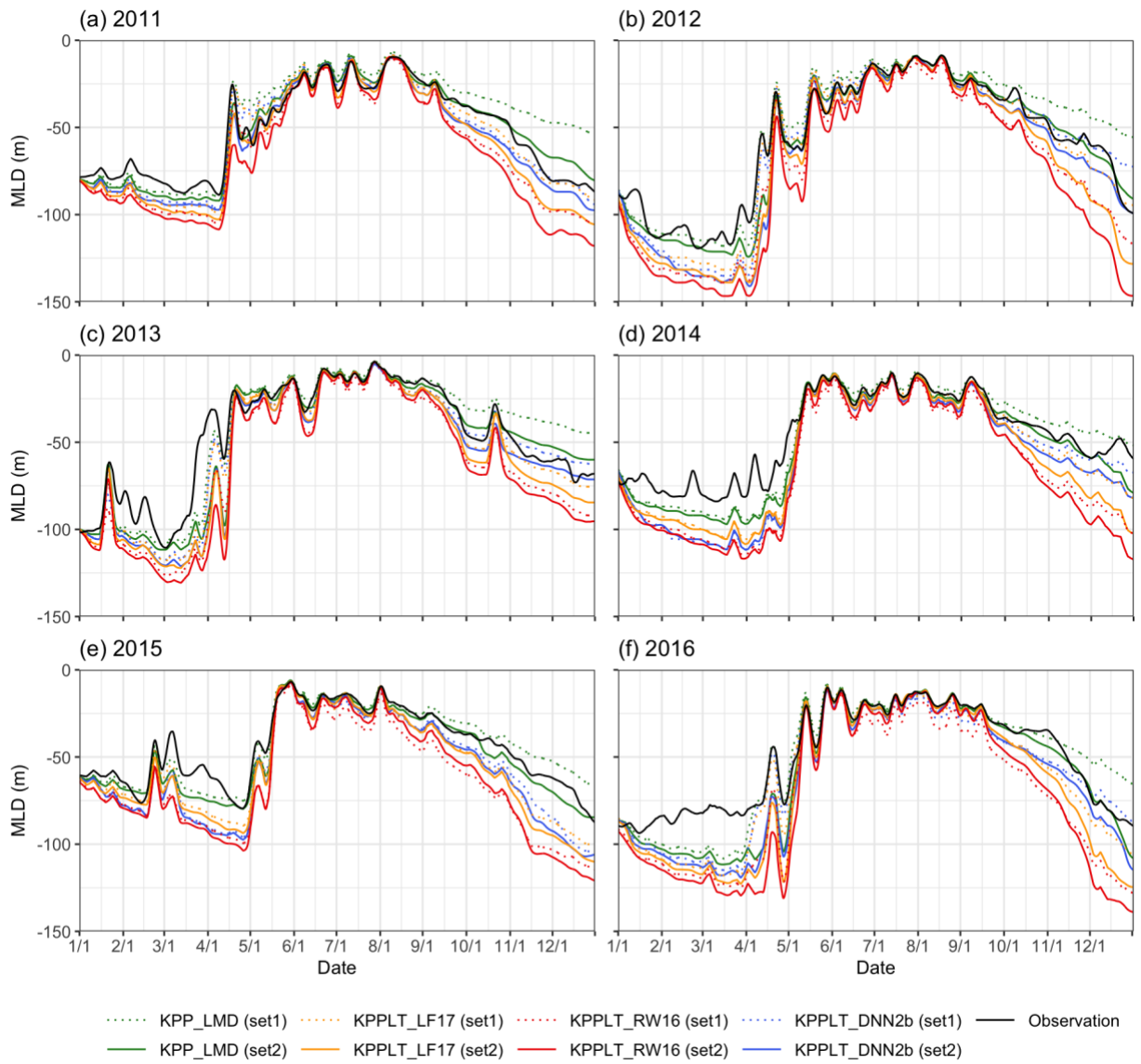

Figure 7. Comparison of simulated MLDs between GOTM simulations using PMEL derived flux products and those using COARE-v3.6 online calculated fluxes. The MLDs were diagnosed by the depth where water density exceeds surface water density by $0.03 kg/m^3$. For clarity in demonstrating long-term trends and reducing the impact of short-term fluctuations, MLDs were smoothed using a 5-day running average.

522 **5.2 Comparison of the velocity scale coefficient and the unresolved shear coefficient**

523 Figure 8 presents the dependence of the velocity scale coefficient (ϵ in Equation 5) on
524 turbulent Langmuir number and MLD and compares it across KPPLT_LF17, KPPLT_RW16,
525 and KPP_DNN2b.

526 In all three schemes, the magnitude of ϵ shows a clear dependence on the non-
527 dimensional turbulent Langmuir number (La_t). Specifically, a smaller La_t is associated with a
528 larger ϵ, indicating wave-induced turbulence has a larger effect on mixing. ϵ by KPPLT_RW16
529 (Figures 8c and 8d) is the largest among the three schemes. ϵ by KPP_DNN2b displays a
530 dependence on the MLD as well. The deeper the MLD, the larger the ϵ.

531

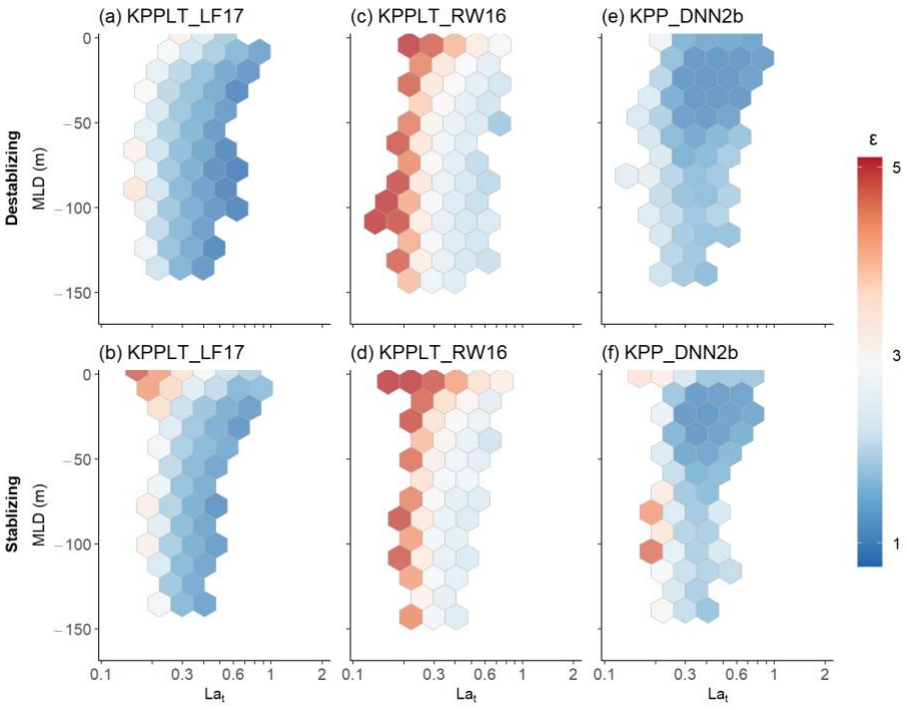

532

533 **Figure 8.** Comparison of the velocity scales coefficient (ϵ) as computed by two of the
534 deterministic KPPLT schemes, i.e., KPPLT_LF17 (panels a and b) and KPPLT_RW16 (panels c
535 and d), and as predicted by the KPP_DNN2b (panels e and f). The color scale in each hexagon

536 represents the average enhancement of velocity scale ϵ over all data points contained in the
537 hexagon region. Only hexagons averaged over more than 50 data points are shown. The upper
538 row (panels a, b, c) corresponds to conditions of destabilizing buoyancy forces, whereas the
539 lower row (panels d, e, f) represents conditions under stabilizing buoyancy forces. Different from
540 the regime diagrams in Figure 2, the y-axis is the mixed layer depth (MLD).
541
542 Figure 9 shows the unresolved shear coefficient (η in Equation 6) for KPPLT_LF17,
543 KPPLT_RW16, and KPP_DNN2b. As demonstrated in the simulated temperature profiles and
544 SST (Figures 4 and 5), the magnitude of the unresolved shear coefficient η is more important
545 than the magnitude of the velocity scale ϵ coefficient in the simulation of upper-ocean
546 temperature and stratification.
547 For KPPLT_LF17 (Figures 9a and 9b), η only varies with forcing conditions when
548 surface buoyancy forcing is destabilizing. Under stabilizing buoyancy forcing conditions, the
549 velocity scale of unresolved shear U_t^2 by KPPLT_LF17 is the same as that by KPP_LMD, thus
550 $\eta = 1.0$ regardless of the wind-wave-buoyancy condition or MLD. Under destabilizing
551 buoyancy forcing conditions, the average value of η ranges from 1.0 to 2.5, but there is no
552 apparent correlation between η and either La_t or MLD. For KPPLT_RW16 (Figures 9c and 9d),
553 there is an apparent relationship between η and La_t, and no apparent tendency differences under
554 different buoyancy forcing conditions or MLD. The more dominant the wave effect over the
555 wind effect, the smaller the La_t and the larger the η.
556 In KPP_DNN2b (Figures 9e and 9f), η is not only impacted by La_t, but also by MLD and
557 surface buoyancy forcing. Similar to KPPLT_LF17 and KPPLT_RW16, η increases with
558 decreasing turbulence Langmuir number for all MLDs. Different from the two KPPLT schemes,

559 there is an evident relationship between η and MLD: η decreases with increasing MLD.
560 Langmuir circulation arises from wave-current interaction close to the surface, where it exhibits
561 the greatest intensity (e.g., McWilliams et al., 1997). Weller and Price (1988) found no
562 significant wave effect at the base of the mixed layer if the MLD exceeds $-40m$ deep.
563 Furthermore, η also depends on whether the surface buoyancy forcing is stabilizing or
564 destabilizing. For the same La_t and MLD, η is larger when surface buoyancy forcing is
565 stabilizing.

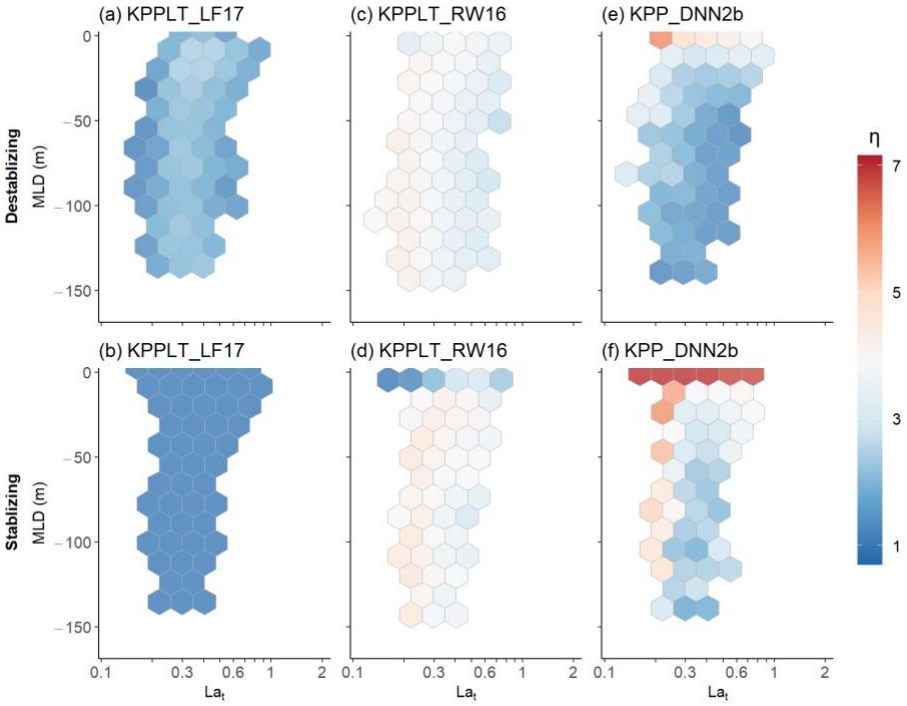

566
567
568 **Figure 9.** Same as Figure 8, but for the unresolved shear coefficient (η)
569

5.3 The Efficiency of KPP_DNNs

A parameterization must be efficient so that it can be used in realistic ocean models for long-term integrations. The efficiency of the KPP_DNNs is evaluated by comparing them with the traditional KPP and KPPLT schemes (refer to Table 1) within the GOTM framework.

simulations were conducted on a dedicated single core of Intel Cascade Lake (Intel® Xeon® Platinum 8260 Processor) CPUs on the Louisiana Optical Network Initiative's high-performance computing server (LONI-HPC). The year 2013 served as the benchmark period for the GOTM model runs to evaluate efficiency. In all simulations, the forcing and configuration were identical. To ensure accuracy in measuring computational efficiency, we disabled output.

The results showed that the run times for KPP_DNNs are comparable with those of traditional KPP and KPPLT schemes. Specifically, the run time for KPP_DNNs exceeds less than 4% that of KPP_LMD and KPPLT_VR12 and is slightly shorter than that for KPPLT_LF17 and KPPLT_RW16. This comparison suggests that KPP_DNN schemes are suitable for implementation in realistic ocean and climate models.

Table 2. List of parameterization names and their run time.

Simulation Name	Run Time (seconds)
KPP_LMD	3.06
KPPLT_VR12	3.07
KPPLT_LF17	3.48
KPPLT_RW16	4.12
KPP_DNN1	3.09
KPP_DNN2a	3.16
KPP_DNN2b	3.20

6 Conclusions

In this study, feedforward deep neural networks (DNNs) tuned using 11-year solutions of turbulence-resolving large eddy simulations (LES) driven by realistic forcing conditions at ocean station Papa (OSP), are used to improve one of the most popular parameterizations for mixing in the ocean surface boundary layer (OSBL), the K-Profile Parameterization (KPP). Specifically, the DNNs are used to parameterize two coefficients, the velocity scale coefficient ϵ and the unresolved shear coefficient η in equations 5 and 6, that revise two uncertain but important parameters in the KPP. The fine-tuned KPP_DNNs are implemented into the general ocean turbulence model (GOTM), a one-dimensional column model serving as a testbed of turbulence parameterization. The KPP_DNNs are compared with seven popular traditional deterministic schemes, including the first-order KPP and the second-moment closure (SMC) schemes within the GOTM using simulations for upper-ocean conditions at OSP between 2011 and 2016. Key conclusions from this study are summarized as follows:

- The KPP_DNNs are stable for integration over several years. They are also efficient and have comparable run time to traditional deterministic KPP schemes.
- When using the pre-derived flux productions, the simulated mixed layer is the warmest and the shallowest using the schemes without wave effects, i.e., KPP_LMD, and SMC, i.e., SMC_KC94. The simulated re-stratification in spring is faster in SMC than in KPP.
- With the addition of wave effects, i.e., using KPPLTs, SMCLT, KPP_DNN2a and KPP_DNN2b, the simulated mixed layer tends to be cooler and deeper. The simulated mixed layer is the coolest and the deepest using KPPLT_RW16.
- Biases in the simulated SST are smaller when using a bulk flux to calculate buoyancy flux online (Simulation set 2) than when using pre-calculated flux (Simulation set 1).

However, biases in the simulated MLDs are larger when using the on-line buoyancy flux calculation.

- In the KPP framework, the unresolved shear coefficient η shall be considered simultaneously with the velocity scale coefficient ϵ. Impacts on the simulated sea surface temperature (SST) and mixed layer depth (MLD) are limited if only ϵ is considered.
- In all KPPLT_LF17, KPPLT_RW16 and KPP_DNN2b, the magnitude of ϵ is impacted by the relative strength of wave effect. The more dominant the wave effect, the smaller the turbulent Langmuir number (La_t), the larger the ϵ.
- In KPP_DNN2, the value of η also changes with the thickness of mixed layer and whether the surface buoyancy forcing is stabilizing or destabilizing. η is much larger if the mixed layer is shallow but decreases fast with the increasing of MLD. When MLD and La_t are identical, η is smaller when surface buoyancy forcing is destabilizing than stabilizing.

The KPP_DNN schemes not only reproduce the dependence of turbulent mixing on Langmuir number, but also uncover the correlation with the MLD and whether the surface buoyancy forcing is stabilizing or destabilizing. This study highlights the potential of leveraging deep learning to identify and incorporate complex, multifaceted influences on turbulent mixing in the OSBL,

The next step involves implementing and evaluating the KPP_DNNs in a realistic ocean model for a regional ocean. Although KPP_DNN2a does not include waves as an input, it implicitly includes wave-induced mixing as it is trained using LES solutions with wave effects. Given its reasonable results and its simplicity without the need to couple the ocean model with a wave model, it would be the first choice. We are currently conducting LES simulations for the

633 Gulf of Mexico and will train the KPP_DNNs using those simulations. The KPP_DNN2a will be
634 implemented in the HYCOM model configured for the Gulf of Mexico (Dukhovskoy et al.,
635 2015; Laxenaire et al., 2023).

636 **Acknowledgments**

637 JY and JHL were supported by the Office and Naval Research through grant N00014-23-1-2553.
638 EC and OZ were supported by the Office of Naval Research through grant N00014-23-1-2547.
639 Computation was performed at supercomputers provided by the high-performance computing at
640 Louisiana State University and Louisiana Optical Network Initiative (LONI). This is PMEL
641 publication #5622.

642

643 **Open Research**

644 The observed temperature and salinity profiles, the forcing data, the derived surface fluxes at
645 OSP can be downloaded from the Pacific Marine Environmental Laboratory website
646 (https://www.pmel.noaa.gov/ocs/data/disdel/). The GOTM codes with KPP_DNN model and
647 COARE bulk flux algorithm implemented are available at
648 https://github.com/lsuocean/KPP_DNN_in_GOTM.

649

650 **References**

651 Abolfazli, E., Liang, J. H., Fan, Y. L., Chen, Q. J., Walker, N. D., & Liu, J. L. (2020). Surface Gravity Waves and
652 Their Role in Ocean-Atmosphere Coupling in the Gulf of Mexico. *Journal of Geophysical Research-*
653 *Oceans, 125*(7), e2018JC014820. https://doi.org/10.1029/2018JC014820
654 Adcroft, A., Anderson, W., Balaji, V., Blanton, C., Bushuk, M., Dufour, C. O., et al. (2019). The GFDL Global
655 Ocean and Sea Ice Model OM4.0: Model Description and Simulation Features. *Journal of Advances in*
656 *Modeling Earth Systems, 11*(10), 3167-3211. https://doi.org/10.1029/2019MS001726

Ali, A., Christensen, K. H., Breivik, O., Malila, M., Raj, R. P., Bertino, L., et al. (2019). A comparison of Langmuir turbulence parameterizations and key wave effects in a numerical model of the North Atlantic and Arctic Oceans. *Ocean Modelling, 137*, 76-97. https://doi.org/10.1016/j.ocemod.2019.02.005

Barnier, B., Siefridt, L., & Marchesiello, P. (1995). Thermal forcing for a global ocean circulation model using a three-year climatology of ECMWF analyses. *Journal of Marine Systems, 6*(4), 363-380. https://doi.org/10.1016/0924-7963(94)00034-9

Belcher, S. E., Grant, A. L. M., Hanley, K. E., Fox-Kemper, B., Van Roekel, L., Sullivan, P. P., et al. (2012). A global perspective on Langmuir turbulence in the ocean surface boundary layer. *Geophysical Research Letters, 39*(18). https://doi.org/10.1029/2012GL052932

Bodner, A. S., Fox-Kemper, B., Johnson, L., Van Roekel, L. P., McWilliams, J. C., Sullivan, P. P., et al. (2023). Modifying the Mixed Layer Eddy Parameterization to Include Frontogenesis Arrest by Boundary Layer Turbulence. *Journal of Physical Oceanography, 53*(1), 323-339. https://doi.org/10.1175/JPO-D-21-0297.1

Bodner, A. S., Fox-Kemper, B., Van Roekel, L. P., McWilliams, J. C., & Sullivan, P. P. (2020). A perturbation approach to understanding the effects of turbulence on frontogenesis. *Journal of Fluid Mechanics, 883*, A25. https://doi.org/10.1017/jfm.2019.804

Bond, N. A., Cronin, M. F., Freeland, H., & Mantua, N. (2015). Causes and impacts of the 2014 warm anomaly in the NE Pacific. *Geophysical Research Letters, 42*(9), 3414-3420. https://doi.org/10.1002/2015GL063306

Brenowitz, N. D., & Bretherton, C. S. (2018). Prognostic Validation of a Neural Network Unified Physics Parameterization. *Geophysical Research Letters, 45*(12), 6289-6298. https://doi.org/10.1029/2018GL078510

Burchard, H., Bolding, K., & Villarreal, M. R. (1999). *GOTM, a general ocean turbulence model: theory, implementation and test cases*: Space Applications Institute.

Chalikov, D. (2005). Similarity theory and parameterization of mixing in the upper ocean. *Environmental Fluid Mechanics, 4*, 385-414. https://doi.org/10.1007/s10652-005-5489-6

Chassignet, E. P., Yeager, S. G., Fox-Kemper, B., Bozec, A., Castruccio, F., Danabasoglu, G., et al. (2020). Impact of horizontal resolution on global ocean-sea-ice model simulations based on the experimental protocols of the Ocean Model Intercomparison Project phase 2 (OMIP-2). *Geoscientific Model Development Discussions, 2020*, 1-58. https://doi.org/10.5194/gmd-13-4595-2020

Craig, P. D., & Banner, M. L. (1994). Modeling Wave-Enhanced Turbulence in the Ocean Surface-Layer. *Journal of Physical Oceanography, 24*(12), 2546-2559. https://doi.org/10.1175/1520-0485(1994)024<2546:MWETIT>2.0.CO;2

Cronin, M. F., Anderson, N. D., Zhang, D., Berk, P., Wills, S. M., Serra, Y., et al. (2023). PMEL Ocean Climate Stations. *Oceanography, 36*(2/3), 46-53. https://www.jstor.org/stable/27257879

Cronin, M. F., Pelland, N. A., Emerson, S. R., & Crawford, W. R. (2015). Estimating diffusivity from the mixed layer heat and salt balances in the N orth P acific. *Journal of Geophysical Research: Oceans, 120*(11), 7346-7362. https://doi.org/10.1002/2015JC011010

693 Di Lorenzo, E., & Mantua, N. (2016). Multi-year persistence of the 2014/15 North Pacific marine heatwave. *Nature*
694 *Climate Change*, *6*(11), 1042-1047. https://doi.org/10.1038/nclimate3082
695 Dukhovskoy, D. S., Leben, R. R., Chassignet, E. P., Hall, C. A., Morey, S. L., & Nedbor-Gross, R. (2015).
696 Characterization of the uncertainty of loop current metrics using a multidecadal numerical simulation and
697 altimeter observations. *Deep Sea Research Part I: Oceanographic Research Papers*, *100*, 140-158.
698 https://doi.org/10.1016/j.dsr.2015.01.005
699 Fan, Y. L., Jarosz, E., Yu, Z. T., Rogers, W. E., Jensen, T. G., & Liang, J. H. (2018). Langmuir turbulence in
700 horizontal salinity gradient. *Ocean Modelling*, *129*, 93-103. https://doi.org/10.1016/j.ocemod.2018.07.010
701 Fox-Kemper, B., Adcroft, A., Böning, C. W., Chassignet, E. P., Curchitser, E., Danabasoglu, G., et al. (2019).
702 Challenges and Prospects in Ocean Circulation Models. *Frontiers in Marine Science*, *6*, 65.
703 https://doi.org/10.3389/fmars.2019.00065
704 Fox-Kemper, B., Bachman, S., Pearson, B., & Reckinger, S. (2014). Principles and advances in subgrid modelling
705 for eddy-rich simulations. *Clivar Exchanges*, *19*(2), 42-46.
706 Gagne, D. I. I., Christensen, H. M., Subramanian, A. C., & Monahan, A. H. (2020). Machine Learning for Stochastic
707 Parameterization: Generative Adversarial Networks in the Lorenz '96 Model. *Journal of Advances in*
708 *Modeling Earth Systems*, *12*(3), e2019MS001896. https://doi.org/10.1029/2019MS001896
709 Gaspar, P., Gregoris, Y., & Lefevre, J. M. (1990). A Simple Eddy Kinetic-Energy Model for Simulations of the
710 Oceanic Vertical Mixing - Tests at Station Papa and Long-Term Upper Ocean Study Site. *Journal of*
711 *Geophysical Research-Oceans*, *95*(C9), 16179-16193. https://doi.org/10.1029/JC095iC09p16179
712 Gentine, P., Pritchard, M., Rasp, S., Reinaudi, G., & Yacalis, G. (2018). Could machine learning break the
713 convection parameterization deadlock? *Geophysical Research Letters*, *45*(11), 5742-5751.
714 https://doi.org/10.1029/2018GL078202
715 Gulli, A., & Pal, S. (2017). *Deep learning with Keras*: Packt Publishing Ltd.
716 Hanley, K. E., Belcher, S. E., & Sullivan, P. P. (2010). A global climatology of wind–wave interaction. *Journal of*
717 *Physical Oceanography*, *40*(6), 1263-1282. https://doi.org/10.1175/2010JPO4377.1
718 Harcourt, R. R. (2015). An Improved Second-Moment Closure Model of Langmuir Turbulence. *Journal of Physical*
719 *Oceanography*, *45*(1), 84-103. https://doi.org/10.1175/JPO-D-14-0046.1
720 Jerlov, N. G. (1976). *Marine optics*: Elsevier.
721 Kantha, L. H., & Clayson, C. A. (1994). An Improved Mixed-Layer Model for Geophysical Applications. *Journal of*
722 *Geophysical Research-Oceans*, *99*(C12), 25235-25266. https://doi.org/10.1029/94JC02257
723 Ketkar, N., & Ketkar, N. (2017). Introduction to keras. *Deep learning with python: a hands-on introduction*, 97-111.
724 Kukulka, T., Plueddemann, A. J., Trowbridge, J. H., & Sullivan, P. P. (2009). Significance of Langmuir circulation
725 in upper ocean mixing: Comparison of observations and simulations. *Geophysical Research Letters*,
726 *36*(10). https://doi.org/10.1029/2009GL037620
727 Large, W. G., Mcwilliams, J. C., & Doney, S. C. (1994). Oceanic Vertical Mixing - a Review and a Model with a
728 Nonlocal Boundary-Layer Parameterization. *Reviews of Geophysics*, *32*(4), 363-403.
729 https://doi.org/10.1029/94RG01872

Laxenaire, R., Chassignet, E. P., Dukhovskoy, D. S., & Morey, S. L. (2023). Impact of upstream variability on the Loop Current dynamics in numerical simulations of the Gulf of Mexico. *Frontiers in Marine Science, 10*, 1080779. https://doi.org/10.3389/fmars.2023.1080779

Li, Q., & Fox-Kemper, B. (2017). Assessing the Effects of Langmuir Turbulence on the Entrainment Buoyancy Flux in the Ocean Surface Boundary Layer. *Journal of Physical Oceanography, 47*(12), 2863-2886. https://doi.org/10.1175/JPO-D-17-0085.1

Li, Q., Reichl, B. G., Fox-Kemper, B., Adcroft, A. J., Belcher, S. E., Danabasoglu, G., et al. (2019). Comparing Ocean Surface Boundary Vertical Mixing Schemes Including Langmuir Turbulence. *Journal of Advances in Modeling Earth Systems, 11*(11), 3545-3592. https://doi.org/10.1029/2019MS001810

Li, Q., Webb, A., Fox-Kemper, B., Craig, A., Danabasoglu, G., Large, W. G., & Vertenstein, M. (2016). Langmuir mixing effects on global climate: WAVEWATCH III in CESM. *Ocean Modelling, 103*, 145-160. https://doi.org/10.1016/j.ocemod.2015.07.020

Li, Y., Yang, R., Yang, C., Yu, M., Hu, F., & Jiang, Y. (2017). Leveraging LSTM for rapid intensifications prediction of tropical cyclones. *ISPRS annals of photogrammetry, remote sensing & spatial information sciences, 4*, 101-105. https://doi.org/10.5194/isprs-annals-IV-4-W2-101-2017

Liang, J. H., Deutsch, C., McWilliams, J. C., Baschek, B., Sullivan, P. P., & Chiba, D. (2013). Parameterizing bubble-mediated air-sea gas exchange and its effect on ocean ventilation. *Global Biogeochemical Cycles, 27*(3), 894-905. https://doi.org/10.1002/gbc.20080

Liang, J. H., Emerson, S. R., D'Asaro, E. A., McNeil, C. L., Harcourt, R. R., Sullivan, P. P., et al. (2017). On the role of sea-state in bubble-mediated air-sea gas flux during a winter storm. *Journal of Geophysical Research-Oceans, 122*(4), 2671-2685. https://doi.org/10.1002/2016JC012408

Liang, J. H., Yuan, J. G., Wan, X. L., Liu, J. L., Liu, B. Q., Jang, H., & Tyagi, M. (2022). Exploring the use of machine learning to parameterize vertical mixing in the ocean surface boundary layer. *Ocean Modelling, 176*, 102059. https://doi.org/10.1016/j.ocemod.2022.102059

Liu, J., Yuan, J., & Liang, J.-H. (2022). An evaluation of vertical mixing parameterization of ocean boundary layer turbulence for cohesive sediments. *Deep Sea Research Part II: Topical Studies in Oceanography, 204*, 105168. https://doi.org/10.1016/j.dsr2.2022.105168

McWilliams, J. C., Huckle, E., Liang, J. H., & Sullivan, P. P. (2014). Langmuir Turbulence in Swell. *Journal of Physical Oceanography, 44*(3), 870-890. https://doi.org/10.1175/JPO-D-13-0122.1

McWilliams, J. C., & Sullivan, P. P. (2000). Vertical mixing by Langmuir circulations. *Spill Science & Technology Bulletin, 6*(3-4), 225-237. https://doi.org/10.1016/S1353-2561(01)00041-X

McWilliams, J. C., Sullivan, P. P., & Moeng, C. H. (1997). Langmuir turbulence in the ocean. *Journal of Fluid Mechanics, 334*, 1-30. https://doi:10.1017/S0022112096004375

Ott, J., Pritchard, M., Best, N., Linstead, E., Curcic, M., & Baldi, P. (2020). A Fortran-Keras Deep Learning Bridge for Scientific Computing. *Scientific Programming, 2020*, 1-13. https://doi.org/10.1155/2020/8888811

765 Paulson, C. A., & Simpson, J. J. (1977). Irradiance measurements in the upper ocean. *Journal of Physical*
766 *Oceanography, 7*(6), 952-956. https://doi.org/10.1175/1520-
767 0485(1977)007%3C0952:IMITUO%3E2.0.CO;2
768 Pearson, B. C., Grant, A. L. M., Polton, J. A., & Belcher, S. E. (2015). Langmuir Turbulence and Surface Heating in
769 the Ocean Surface Boundary Layer. *Journal of Physical Oceanography, 45*(12), 2897-2911.
770 https://doi.org/10.1175/JPO-D-15-0018.1
771 Rasp, S. (2020). Coupled online learning as a way to tackle instabilities and biases in neural network
772 parameterizations: general algorithms and Lorenz 96 case study (v1.0). *Geoscientific Model Development,*
773 *13*(5), 2185-2196. https://doi.org/10.5194/gmd-13-2185-2020
774 Rasp, S., Pritchard, M. S., & Gentine, P. (2018). Deep learning to represent subgrid processes in climate models.
775 *Proceedings of the National Academy of Sciences, 115*(39), 9684-9689.
776 https://doi.org/10.1073/pnas.1810286115
777 Reichl, B. G., & Hallberg, R. (2018). A simplified energetics based planetary boundary layer (ePBL) approach for
778 ocean climate simulations. *Ocean Modelling, 132*, 112-129. https://doi.org/10.1016/j.ocemod.2018.10.004
779 Reichl, B. G., Wang, D., Hara, T., Ginis, I., & Kukulka, T. (2016). Langmuir Turbulence Parameterization in
780 Tropical Cyclone Conditions. *Journal of Physical Oceanography, 46*(3), 863-886.
781 https://doi.org/10.1175/JPO-D-15-0106.1
782 Sane, A., Reichl, B. G., Adcroft, A., & Zanna, L. (2023). Parameterizing Vertical Mixing Coefficients in the Ocean
783 Surface Boundary Layer Using Neural Networks. *Journal of Advances in Modeling Earth Systems, 15*(10).
784 https://doi.org/10.1029/2023MS003890
785 Sinha, N., Tejada-Martínez, A. E., Akan, C., & Grosch, C. E. (2015). Toward a K-Profile Parameterization of
786 Langmuir Turbulence in Shallow Coastal Shelves. *Journal of Physical Oceanography, 45*(12), 2869-2895.
787 <Go to ISI>://WOS:000366394100001
788 Skyllingstad, E. D., & Denbo, D. W. (1995). An Ocean Large-Eddy Simulation of Langmuir Circulations and
789 Convection in the Surface Mixed-Layer. *Journal of Geophysical Research-Oceans, 100*(C5), 8501-8522.
790 https://doi.org/10.1029/94JC03202
791 Sullivan, P. P., & McWilliams, J. C. (2010). Dynamics of Winds and Currents Coupled to Surface Waves. *Annual*
792 *Review of Fluid Mechanics, 42*, 19-42. https://doi.org/10.1146/annurev-fluid-121108-145541
793 Thomson, J., D'Asaro, E. A., Cronin, M. F., Rogers, W. E., Harcourt, R. R., & Shcherbina, A. (2013). Waves and
794 the equilibrium range at Ocean Weather Station P. *Journal of Geophysical Research-Oceans, 118*(11),
795 5951-5962. https://doi.org/10.1002/2013JC008837
796 Thomson, R. E., & Tabata, S. (1987). Steric Height Trends at Ocean Station Papa in the Northeast Pacific-Ocean.
797 *Marine Geodesy, 11*(2-3), 103-113. https://doi.org/10.1080/15210608709379553
798 Troen, I., & Mahrt, L. (1986). A Simple-Model of the Atmospheric Boundary-Layer - Sensitivity to Surface
799 Evaporation. *Boundary-Layer Meteorology, 37*(1-2), 129-148. https://doi.org/10.1007/BF00122760
800 Umlauf, L., & Burchard, H. (2003). A generic length-scale equation for geophysical turbulence models. *Journal of*
801 *Marine Research, 61*(2), 235-265.

van Roekel, L. P., Adcroft, A. J., Danabasoglu, G., Griffies, S. M., Kauffman, B., Large, W., et al. (2018). The KPP boundary layer scheme for the ocean: Revisiting its formulation and benchmarking one-dimensional simulations relative to LES. *Journal of Advances in Modeling Earth Systems, 10*(11), 2647-2685. https://doi.org/10.1029/2018MS001336

van Roekel, L. P., Hamlington, P. E., & Fox-Kemper, B. (2012). *Multiscale simulations of Langmuir cells and submesoscale eddies using XSEDE resources.* Paper presented at the Proceedings of the 1st Conference of the Extreme Science and Engineering Discovery Environment: Bridging from the eXtreme to the Campus and Beyond.

Vertenstein, M., Craig, T., Middleton, A., Feddema, D., & Fischer, C. (2012). CESM1. 0.4 user's guide. *UCAR Doc, 146*.

Warner, J. C., Sherwood, C. R., Arango, H. G., & Signell, R. P. (2005). Performance of four turbulence closure models implemented using a generic length scale method. *Ocean Modelling, 8*(1-2), 81-113. https://doi.org/10.1016/j.ocemod.2003.12.003

Weller, R. A., & Price, J. F. (1988). Langmuir Circulation within the Oceanic Mixed Layer. *Deep-Sea Research Part a-Oceanographic Research Papers, 35*(5), 711-747. https://doi.org/10.1016/0198-0149(88)90027-1

Whitney, F., & Tortell, P. (2006). Fifty years of ocean observations in the Pacific Northeast. In: Wiley Online Library.

Yuan, J. G., & Liang, J. H. (2021). Wind- and Wave-Driven Ocean Surface Boundary Layer in a Frontal Zone: Roles of Submesoscale Eddies and Ekman-Stokes Transport. *Journal of Physical Oceanography, 51*(8), 2655-2680. https://doi.org/10.1175/JPO-D-20-0270.1

Zhu, Y., Zhang, R.-H., Moum, J. N., Wang, F., Li, X., & Li, D. (2022). Physics-informed deep-learning parameterization of ocean vertical mixing improves climate simulations. *National Science Review, 9*(8), nwac044. https://doi.org/10.1093/nsr/nwac044